Journal of Materials Chemistry A

Understanding the Electrochemical Potential and Diffusivity of MnO/C Nanocomposites at Various Charge/discharge States

Journal:	*Journal of Materials Chemistry A*
Manuscript ID	TA-ART-01-2019-000056
Article Type:	Paper
Date Submitted by the Author:	03-Jan-2019

Complete List of Authors:	Liu, Chaofeng; University of Washington, Materials Science and Engineering Fu, Haoyu; Beijing Institute of Nanoenergy and Nanosystems Pei, Yanyan; University of Washington Wu, Jiandong; North Minzu University, School of Materials Science and Engineering Pisharodi, Vivek; University of Washington, Hu, Yang; University of Washington Gao, Guohua; Tongji University, Pohl Institute of Solid State Physics Yang, Robert J.; University of Washington, Materials Science and Engineering Yang, Jihui; University of Washington, Materials Science and Engineering Cao, Guozhong; University of Washington, Materials Science and Engineering

Understanding the Electrochemical Potential and Diffusivity of MnO/C Nanocomposites at Various Charge/discharge States

Chaofeng Liu[1], Haoyu Fu[2], Yanyan Pei[1], Jiandong Wu[3], Vivek Pisharodi[1], Yang Hu[1], Guohua Gao[4], Robert J. Yang[1], Jihui Yang[1]* and Guozhong Cao[1]*

1Department of Materials Science and Engineering, University of Washington, Seattle, WA 98195, USA

2 Beijing Institute of Nanoenergy and Nanosystems, Chinese Academy of Sciences, Beijing, 100083, China

3 School of Materials Science and Engineering, North Minzu University, Yinchuan, 750021, China

4 Shanghai Key Laboratory of Special Artificial Microstructure, Tongji University, Shanghai, 200092, China

*Corresponding authors (G.Z. Cao, Email: gzcao@uw.edu and J.H. Yang, jihuiy@uw.edu)

Abstract

Li-ion diffusion and lithiation kinetics in MnO/C nanocomposites were systematically investigated through monitoring the change in charge transfer resistance and the ion diffusion coefficient and the kinetically predominant process at various charge/discharge states. Crystal field analysis and density functional theory (DFT) calculations were introduced to reveal the relationship among electronic structure of the phase compositions and the displayed electrochemical potential and its profile. The split 3*d* orbitals in Mn ion determines the ordering of electron migration and energy difference, leading to the different potential profiles in the lithiated/delithiated process. Phase compositions strongly affected the intrinsic properties of the MnO/C nanocomposites makes the ion diffusion coefficient increases from ~10^{-15} to 10^{-11} cm^2 s^{-1} when the electrode progresses from the fully charged to fully discharged state, while both surface redox reaction and solid-state diffusion can be the limiting process depending on the states of lithiation/delithiation. In addition, the MnO/C anode delivers an energy efficiency of 90% in a Li-ion hybrid capacitor, suggesting a promising and competitive application in the future.

Keywords: electrochemical potential, solid state diffusion, MnO, impedance, Li-ion capacitor

Introduction

Advancements in harvesting renewable energy have been driven by the environmental concerns from the utilization of the fossil fuels.[1] Energy storage devices have rapidly spread in the forms such as smart electronics, electric vehicles, and smart grid stations; and have become increasingly indispensable components in the modern society. Rechargeable batteries and supercapacitors are the main energy storage devices in which electrode materials store ions and electrons and convert electricity into chemical energy reversibly in the charge/discharge processes.[2] Electrode materials, in general, store energy through three mechanisms: intercalation, alloying, and conversion.[3, 4] Intercalation anode materials always possess working voltage plateaus,[5, 6] though the limited active sites in the host lattices restrict the energy densities of full batteries.[7] Alloying materials react with Li ions to form the alloy phases [8, 9] which leads to rapid pulverization from the typically huge volume expansion.[10, 11] Conversion materials are formed through the breakdown and recombination of chemical bonds in the energy storage reactions.[12, 13] The theoretical specific capacity and volume expansion of conversion materials are in between those of intercalation and alloying materials.[14, 15] In transition metal oxides,[16] sulfides,[17] phosphides, [18] and selenides, [19] the metallic transition elements as well as the products consisting of alkaline ions and the anions from the host materials will be separated during the discharge processes.

In terms of transition metal oxides, manganese monoxide (MnO) is an ideal material to study the relationship between structure and electrochemical performance due to its simple cubic crystal structure and its typical voltage profiles with a discharge plateau and sloped charge similar to those of most oxides.[20-22] MnO holds several advantages as an anode material including a relatively high theoretical specific capacity of 756 mA h g^{-1}, a relatively low discharge voltage around 0.5 V, low cost due to its high abundance in the Earth's crust, and low toxicity. MnO anode has been extensively studying for improving the rate capability and cycling stability, and the general strategy has been to design the microstructures for increasing the surface area, introducing the conductive network, and tuning the crystallinity.[23-26] For example, MnO nanocrystallites mechanically anchored by pore-surface terminations of graphene-like carbon nanosheets to form a monolayer

structure delivered a high specific capacity with good stability, and the Li ion capacitor released a high power density of 15 kW kg^{-1} with 76% capacity retention after 5000 cycles.[27] A topochemical approach was used to synthesize porous MnO/C microsphere by removing $ZnCO_3$ in the mixed carbonates, a high specific capacity of 846 mAh g^{-1} was attributed to the controllable pore sizes.[25] However, some challenges still remain for MnO anode in storage applications. The formation of interfaces and interphases and the changes in the chemical bonds of the reactions are complicated. The relationship between the electrochemical diffusion and potential is also important because the diffusion characteristics will affect the rate capability and could create a large potential hysteresis between the charge and discharge voltage profiles, resulting in a significant energy loss.[28] In particular, MnO displays a discharge plateau, yet a sloping charge curve in the reverse reaction as most of transition metal oxides.[24, 29] This profile asymmetry between charge and discharge has a significant effect on the energy efficiency of full batteries.[5]

In this study, MnO was adopted as a model anode to analyze the relationship between electrochemical potential and electronic structure of compositions through the crystal field analysis and DFT calculation. MnO/C composites were synthesized using a hydrothermal method with a subsequent heat treatment involving an inert gas. Apart from the characterizations of the structure and capacitance contribution to the electrochemical performances, cyclic voltammetry (CV) and electrochemical impedance spectroscopy (EIS) were used to monitor the kinetic processes, evolution of charge transfer resistance, and ion diffusion during the charge/discharge processes. On this basis, the change of the interface was analyzed and discussed through simulations of a series of EIS spectra. Moreover, energy efficiency of the MnO/C anode in a hybrid capacitor has been analyzed to demonstrate its potential use and discern underlying challenges.

Results and Discussion

Electrochemical Potential Analysis

Figure 1a shows the potential profiles of the MnO anode as shown in most of reported studies.[24, 30, 31] A potential plateau appears around 0.5 V during the discharge process, but

during the charging process, a sloping curve is displayed. The nature of the conversion reaction of MnO is the breakdown and recombination of the chemical bonds. The bond dissociation energies have an essential impact on the electrochemical potential along with electronegativity of composition elements, which influence the electron distribution and the strength of the chemical bonds. The electron configuration, such as the scheme of Mn (II) in Figure 1b, determines the order and energy of electrons when they jump into or out of the *d* or *f* orbitals during a reaction. MnO works as an anode and decomposes to metallic Mn and Li_2O,

$$MnO + 2Li^+ + 2e^- \leftrightarrow Mn + Li_2O \quad (1)$$

which displays a potential plateau around 0.5 V during the discharge process.[32] Normally, the electrochemical potential is calculated by Gibbs free energy change in the whole reaction, and the free energy change is defined as [33]

$$\Delta G = \Delta H - T\Delta S = \Delta U + P\Delta V - T\Delta S = -nFE^0 \quad (2)$$

the terms $P\Delta V$ from volume change and $T\Delta S$ from configurational change are negligible as they are of the order of 10^{-5} and 10^{-2} eV, respectively. ΔU is the change in internal energy, which can be approximated as 2-3 eV to evaluate ΔG in the reaction when the assumed temperature at 0 K for DFT calculation.[34] Figure 1c shows the crystal structures of materials involved in the conversion reaction of MnO anode, and the lattice parameters are listed in Table S1. The internal energy of each material including the possible products was calculated by density functional theory as shown in Table 1. In order to estimate the possibility of the intercalation reaction happened at the beginning, the possible Li-Mn-O compounds are hypothesized and the positive energy changes verify that the intercalation reaction is impossible to occur in MnO anode. More calculation details are shown in supporting information. The electrochemical potential (E^0), also be called open circuit voltage (OCV) is calculated by the following equation

$$E^0 = -[U^{DFT}(Li_2O) + U^{DFT}(Mn) - U^{DFT}(MnO) - 2U^{DFT}(Li)]/2F \quad (3)$$

The calculated E^0 is 1.5 V that deviates from the experimental discharge voltage as the reported calculation.[35] The deviation between the experimental and theoretical potentials comes from the theoretical calculation using the open circuit voltage and the experimental

reflecting the average. Besides, the configuration entropy was not considered when a new phase nucleated and grew in the host materials, as was the case for the $LiFePO_4$ cathode.[36] Combined with the DFT calculations on the assumed intermediate phases (Calculations details in SI), the results verify that there is difficult to form intercalation or alloying phases in conversion reaction of MnO anode. The chemical bond dissociation energy (BDE) can give an electrochemical potential close to the real state because the nature of a conversion reaction is the breakdown and recombination of chemical bonds. BDE is enthalpy change, but roughly equals to free energy change and would be used to estimate the discharge voltage owing to the volume and configurational change are negligible as mentioned above. The bond energy change in equation (1) can be calculated using the following equation

$$\Delta U_{BDE} = (\Delta U_{Mn-Mn} + 2\Delta U_{Li-O}) - (\Delta U_{Mn-O} + 2\Delta U_{Li-Li}) = -nFE_{BDE} \quad (4)$$

The bond dissociation energies for Mn-O, Li-Li, Mn-Mn, and Li-O are 402, 106, 42, and 341 kJ/mol, respectively.[37] The difference in bond dissociation energies of the MnO conversion reaction is 110 kJ/mol so the potential determined by Equation (4) is 0.57 V, which is very close to the experimental value. The slight difference between the experimental and theoretical calculation of bond energy can be attributed to polarization in the half-cell. However, there is still a big difference between the charging and discharging potential profiles. Most of the transition metal oxides have a visible potential plateau during the discharging process, but they possess sloping profiles that deviate from the calculated results during charging[22, 29] due to electrons jumping in and out of the *d* or *f* orbitals, causing a change in energy. Manganese (Mn) is a multi-electron atom with 7 valence electrons distributed in the 3*d* and 4*s* orbitals, and its metallic state has a cubic structure. The energy level of each orbital influences the electron occupation and the chemical coordination of the cation in its oxides. MnO has a cubic NaCl-type crystal structure where the Mn^{2+} ion coordinates with six oxygens to form an octahedron (Figure 1a inset). The remaining five electrons in Mn^{2+} occupy two sets of 3*d* orbitals with three lower energy t_{2g} orbitals and two higher energy e_g orbitals (Figure 1b). In the DFT calculation, the assumed temperature is 0 K so that the antiferromagnetic (AFM) MnO has a D_{3d} poin-group symmetry,[38] leading to a mixed t_{2g} orbitals so as to show the a_{1g} singlet and the e'_g doublet as the DOS depicted in Figure 1d. The invariant e_g is often

marked by e''_g in D_{3d} symmetry operations. Since O^{2-} belongs to a weak-field ligand, it results in a high-spin crystal field in MnO. During the discharging process, MnO transforms to metallic Mn and Li_2O, which suggests the two incoming electrons will jump into the empty e'_g orbitals to reduce Mn^{2+} to Mn metal. The energy differences for both electrons are the same, therefore, the potential profiles during the discharging process are plateau-shaped. The belief is that at the initial of the charging process, there are no degenerate orbitals in the metallic Mn and the electrons in the 4s orbitals has a higher energy level where the electron cloud overlaps in the 4*s* and 3*d* orbitals. In forming MnO, the Mn(II) ion coordinates with an oxygen octahedron and induces the splitting of 3*d* orbitals. At this moment, the empty 4*s* orbitals have a lower energy level than the e'_g orbital, leading to electrons moving from the e'_g to the 4*s* orbitals. This continuous energy change is manifested as a sloping potential profile during the charging process.[39] The big difference between the charging and discharging potential profiles implies a potential hysteresis that leads to energy losses in a device. The electronegativity of elements influences the strength of chemical bonds and affects the potential hysteresis to some extent. Using the electronegativity values, the ionic character of chemical bonds can be evaluated through the following equation[40]

$$\%\ \text{ionic character} = 1 - 100 \times \exp[-0.25(X_a - X_b)^2] \quad (5)$$

where X_a and X_b are the electronegativity values of the anion and cation, respectively. The electronegativity value of Mn is 1.55 Pauling units and that of O is 3.44 Pauling units. The ionicity in MnO is almost 59.1%, meaning the ionic bond dominates the chemical properties. Figure S1 shows the charge density difference map of Mn-O from the DFT calculations. Mn atoms lose electrons and O atoms receive electrons to form the Mn-O bond. The electron cloud is denser around O ions and no electron cloud overlapping occurs between Mn and O. The higher ionic character in the chemical bond suggests the electrons in the 3*d* orbital have a lower electron sharing tendency which makes the reaction energetics high.[41] In addition, the Pauling electronegativity of Li is 0.98 and the iconicity of the Li-O bond is almost 78.0%. Thus, the strong ionic bond between alkaline ions and anions from transition metal oxides, such as Li_2O, is another possible reason for the electrochemical potential hysteresis. The energy barriers increase during the charging process more than that of the discharge process.[42]

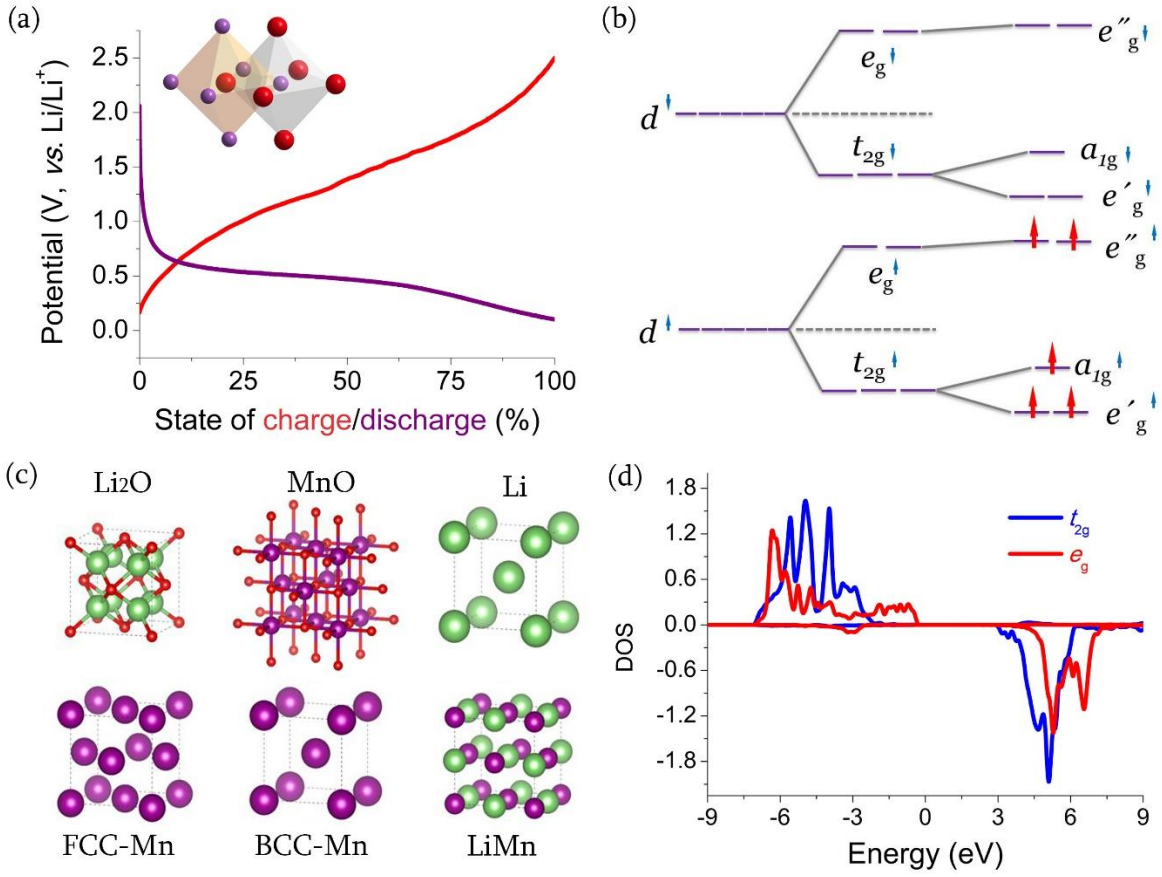

Figure 1. (a) Voltage profile of the MnO anode in a Li-ion half-cell within the voltage window of 0.01-2.5V. The discharging voltage profile shows a plateau around 0.5 V versus Li/Li^+; however, the charging profile is a sloping curve. The inset is the chemical structure of Mn(II) in which the Mn(II) cation and O(II) anion are both octahedral. (b) Schematic of the octahedral crystal field splitting. The 3*d* orbitals in Mn(II) split into two degenerate sets, one containing three orbitals with relatively low energy, and the other set with two orbitals of relatively high energy. Five valence electrons occupy five orbitals separately because the oxygen anion belongs to a weak field ligand. Therefore, it forms a high spin crystal field in MnO. In the DFT calculation, the assumed temperature is 0 K, MnO stays with the antiferromagnetic (AFM) state and the orbitals go through the secondary splitting because the *D*3d point-group symmetry mixes the *t*2g so as to show the a_{1g} singlet and e'_g doublet. (c) The crystal structures of Li_2O, MnO, metallic Li, FCC-Mn, BCC-Mn, and LiMn for internal energies and voltage calculations. (d) Density of states of e_g and t_{2g} orbitals of Mn(II) ion in AFM state which is in accord with the mixed splitting orbitals in schematic b.

Table 1. The internal energy in a cell contained one chemical formula of matter (unit: eV)

MnO	Li	Li_2O	FCC-Mn	BCC-Mn	LiMn	LiMnO	Li_2MnO
-16.406	-1.903	-14.313	-8.900	-8.839	-7.996	-15.811	-17.356

Materials Characterizations

Figure 2a shows X-ray diffraction (XRD) patterns of the resulting samples before and after calcination. The sample obtained from the solvothermal synthesis can be indexed with the standard XRD pattern of manganese carbonate ($MnCO_3$, space group, R-3C, hexagonal, 4.7901×4.7901×15.694Å, PDF card 44-1472) which has a calcite-like structure with Mn(II) exhibiting an octahedral coordination with the anion ligands. More importantly, the formation of the carbonate suggests that glucose was oxidized to the carbonate group during the solvothermal reactions and combined with the Mn cations. Thermogravimetric analysis/ differential scanning calorimetry (TGA/DSC) curves reveal the thermal decomposition of $MnCO_3$ in Figure S2 that displays an endothermal peak at 400˚C, implying a decomposition reaction. The drop shown on the TGA curve can be attributed to the release of carbon dioxide. To ensure a complete decomposition and good graphitization of the residual carbon, the solvothermal product was calcined at 650 ˚C for 2 h with nitrogen gas. After the calcination, the main phase transformed into manganese monoxide (MnO, space group Fm-3m, cubic, a=4.445Å, PDF 07-0230) which adopts a rock-salt structure where the cation and anion both have the octahedral coordination (Figure S3). The XRD pattern shows peaks corresponding to MnO, as shown in Figure 2a. Microstructure of the calcined MnO sample looks like batches of grasses where the length of a batch is around 1 μm and the diameter is approximately 400 nm (Figure 2b). All have uniform size and morphology. Each of them consists of numerous nanoparticles as revealed by the transmission electron microscopy (TEM) image in Figure 2c. The center of a single nano-batch is darker than the edges because the center of the three-dimensional batch is thicker in comparison with the edges so that the electrons are difficult to transmit through. The local area marked by a green rectangle (Figure 2d) was magnified and it was found that crystalline MnO nanoparticles (~6 nm) were encapsulated in the disordered carbon matrix. The apparent lattice fringes, with inter-planar spacing of 2.57 and 2.23 Å, observed in a high-resolution transmission electron microscopy (HRTEM) agree with the planar distances of the (111) and (200) in MnO (Figure 2d). The energy dispersive spectrum was also collected through energy-dispersive X-ray spectroscopy (EDS) attached to the TEM. The elemental composition consisted of Mn, O and C are in accordance with the XRD results and the elements contained in the raw materials. EDS mappings in Figure 2f-h present the elemental distribution consistent with the batch-like particle shape in Figure 2c. The carbonization of glucose provides the final carbon network in the calcinated sample. Raman spectrum of the sample was collected and the peak fitting was conducted with the Gaussian function for the *D*- and *G*-bands and the Lorentzian function for the additional *I* and *D″* bands (Figure 2i). The *D*-band located around 1339 cm^{-1} originates from a double resonance process involving a phonon and a defect, which implies the carbon is disordered. The *G*-band at

~1589 cm^{-1} stems from in-plane vibrations and has the E_{2g} symmetry that denotes the graphitization of carbon. The *I* band at ~1180 to 1290 cm^{-1} relates to the disorder in the graphitic lattice, which can be attributed to the sp^2-sp^3 bonds or the presence of polyenes. The *D″* band at ~1500 cm^{-1} associated with interstitial defects in disordered sp^2 bonds implies the carbon being amorphous.[43, 44] The ratio of the intensity between the *D*- and the *G*-band *I*(D)/*I*(G) is 0.94 which suggests that the carbon in the calcined sample is in an amorphous state. The carbon content obtained from the DSC/TG curves is 25.5% (Figure S4) and the electrical conductivity determined by a four-point probe direct current technique is 106 S m^{-1}, enough to ensure that charges are transferred in the electrochemical reactions. Additionally, the nitrogen adsorption isotherm was used to determine the specific surface area through the Barrett-Joyner-Halenda (BJH) method, which was found to be 202.2 m^2 g^{-1} with the pore size distribution peak appearing at 4 nm (Figure 2j). The hysteresis loop between the adsorption and desorption branches imply capillary condensation occurred within the mesoporous structure. Assuming that the MnO nanoparticles have a spherical shape with a diameter of 6 nm and the theoretical density of MnO is 5.36 g cm-^{3}, the calculated surface area should be 93.2 m^2 g^{-1}. The big difference between the experimental and calculated values suggests the batch-like MnO/C has porous nanostructures. We speculate this is because the decomposition of $MnCO_3$ releases CO_2 which helps produce more pores in the carbon coating and more MnO nanoparticles during the calcination process.

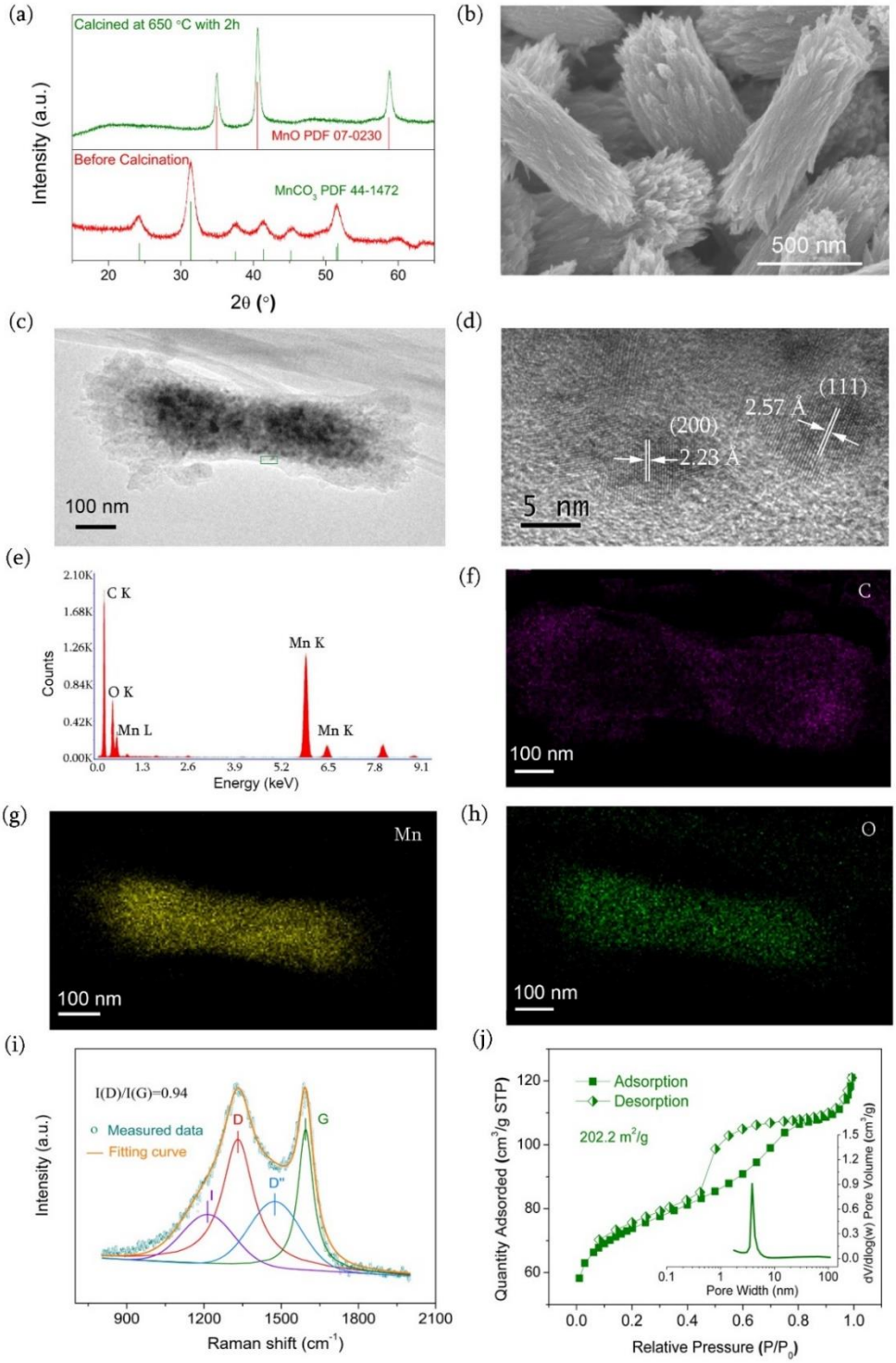

Figure 2. (a) XRD patterns of the sample before and after calcination. The sample derived from the solvothermal synthesis is rhodochrosite $MnCO_3$ and it transforms to the rock salt structure after calcination at 650 ˚C. (b) SEM image of the calcined sample MnO/C that grows in a batch-like shape. (c) TEM image of a single batch-like nano-particle and (d) HRTEM image from a local area of the single particle. The lattice spacings verify the structure of MnO/C. (e) EDS

spectrum collected from the single batch particle. The existing elements (Mn, O, C) are in accord with the raw materials. Carbon stems from the added glucose in the synthesis process. (f-h) EDS mapping of C, Mn and O. All of the elements are distributed homogenously within the whole particle. (i) Raman spectrum of the MnO particles. The *D*, *G*, *I* and *D"* bands reflect the graphitization or disordered state of carbon in the calcined sample. (j) Nitrogen sorption isotherm of MnO/C and the pore size distribution. The hysteresis loop in the curves suggests the batch-like MnO particles contain abundant mesopores.

Lithiation Kinetics and Diffusivity

As described in the chracterizations section, MnO/C nanocomposite presents a high electrical conductivity of 106 S m^{-1}, so no conductive additive was added in preparing the electrode in the test electrochemical property and battery performance characterization and analyses. The redox characteristics of MnO/C were tested through a cyclic voltammogram (CV) within a working voltage window of 0.01-3.00 V and at a sweeping rate of 0.1 mV s^{-1}. The CV curves (Figure 3a) show a reducing peak at 0.29 V in the first cycle and it shifts to 0.35 V in the following cycles. In this process, the Mn-O bonds break down and MnO transforms into Mn and Li_2O. In reverse, the oxidizing peaks at 1.22 V overlap during the first three cycles, suggesting MnO is recovered and there is good reactive reversibility in the MnO/C anode. CV curves at various sweeping rates (Figure S5a) were also collected to analyze kinetic characteristics of MnO/C nanocomposite during the lithiation/delithiation processes because nanomaterials always have high specific surface areas that always endow the reaction kinetics with a simultaneous diffusion- and capacitance-controlled process.[45-47] The diffusion component relates to the Faradaic reaction from the Li^+ insertion process, which always occurs in the intercalation, alloying, or conversion reaction. The capacitance component corresponds to the surface Faradaic reaction which can be thought of as that seen for a pseudocapacitance, and the nonfaradaic reaction from the electric double layer capacitance.[48, 49] Both of the latter capacitive contributions can be separated by analyzing the various sweeping rates of CV curves because the measured current i obeys a power law relationship with the sweeping rate v[49, 50]

$$i = av^b \quad (6)$$

where a and b are the adjustable parameters, and the b-value can be calculated from log i vs. log v (Figure S5b-c). A b-value close to 0.5 means that the current primarily stems from the Faradaic diffusion-controlled process, and a b-value of 1.0 implies a capacitance-controlled process from the surface reactions.[45] Figure 3b shows the b-values calculated from the log i - log v relationship at different states of charge/discharge, and it is easily concluded that the b-value varies with the state of the electrode. In the discharge process, surface adsorption and Faradaic reaction happen when the voltage is higher than 2 V so that the b-value close to 1. In this case, the whole process is controlled by ion adsorption onto the surface of the electrode material due to its high surface area as verified by the nitrogen sorption isotherm tests. The conversion reaction starts at 1.5 V and Li ions migrate across the interfaces between the carbon coating and MnO nanoparticles, thus the b-value is around 0.51. The b-values in the voltage window of 0.5-0.8V lie around 0.75, suggesting the Li-ions adsorb at and diffuse across the surface of the MnO nanoparticles. A b-value of 0.49 around 0.3 V signifies a strong diffusion-controlled process relating to the breakdown of chemical bonds, as verified in the CV curve (Figure 3a). After the breakdown of the chemical bonds, the b-value sits between 0.5 and 1.0, implying that charge storage is simultaneously affected by the surface adsorption effect from the porous batch-like nanostructure as well as the diffusion-limited Faradaic reaction from MnO nanoparticles inside. Charged back to 0.3 V, the b-value becomes 0.51, signifying the start of the recombination of Mn and O and the diffusion-controlled reaction process. In the subsequent charging process, the b-values fall within the range of 0.5-1.0, which suggests a mixed contribution from diffusion and capacitance. The diffusion-controlled influence stems from the conversion reaction of MnO, and the capacitance-controlled contribution originates from the surface and interface of the nanostructured MnO/C. A relatively low b-value appears at 1.6 V during the charging process, which corresponds to the interface diffusion between the carbon coating and MnO. The interface between the two phases induces the ion accumulation or double-layer effect storage generated from different ion diffusion rates of the same electric field. From the work of Dunn and his coworkers, the capacitance contribution can be separated from the CV curves because the current (i) at a fixed voltage (V) equals to the sum of capacitive effect (k_1v) and diffusion-controlled contribution ($k_2v^{1/2}$) as described by [50]

$$i(\mathrm{V}) = k_1 v + k_2 v^{1/2} \quad (7)$$

Figure 3c shows that the capacitance contribution approaches 60% in the CV curve at a sweeping rate of 1.0 mV/s, revealing a strong capacitive effect in the nanostructured MnO/C electrode. The large surface area is a possible reason for the high capacitance contribution due to the formation of an electric double layer between the electrolyte and the carbon coating. Since MnO is a semiconductor and carbon is a conductor, the interface between them easily becomes a space charge region to store charges, just as capacitors do.[51] However, this capacitance effect is weak in comparison to that between the electrode and electrolyte. The rate capability of the batch-like MnO/C anode was tested in a half cell where lithium metal was used as the counter electrode and the testing voltage window was 0.01-2.50V (Figure S6a). The first discharge capacity reaches 1215 mAh g^{-1} and the subsequent capacity stabilizes at 1018 mAh g^{-1} at a current densityof 0.2 A g^{-1}, which are higher than the theoretical value of 756 mAh g^{-1} due to the formation of a reversible solid electrolyte interphase (SEI) and the capacitance contribution from interfaces as reported in the literature.[27, 52-54] Normally, SEI formed on the graphite particle surface prevents the co-intercalation of organic solvent molecules for suppressing the exfoliation of graphite flake and consumption of electrolyte for enhancing the cyclic stability in subsequent cycles.[55, 56] However, the poly/gel-like SEI film in transition metal oxide anode are reversible owing to the probably catalytic effect from the oxides, and provides an extra capacity at low voltage region.[53, 54] More details will be further discussed in the following EIS analysis. As the current density increases to 6.4 A g^{-1}, the electrode still delivers a specific capacity of 256 mAh g^{-1}, which is higher than most of the reported results[57, 58] with no conductive carbon added to the electrode. The cycling stability of the electrode was also tested at a current density of 0.8 A g^{-1}. The specific capacity reaches 594 mAh g^{-1} and capacity retention of 80% was observed over 200 cycles (Figure S6b). Table S2 compares the electrochemical performances of the reported MnO anodes with our results. The good rate capability and cycling stability in our work can be ascribed to the improved kinetics that means the shortened ion diffusion path and accelerated charge transfer in MnO/C composite. For examples, the small 6 nm size of the active MnO nanoparticles benefits for the diffusion-controlled processes. The high specific surface area increases the ion exchange sites and the reaction rate. The porous batch-like

nanostructure with interconnected 3-D conductive network ensures excellent charge transfer. All of these effects synergistically improve the reaction kinetics of MnO/C anode and increase its performance in Li-ion half cells.

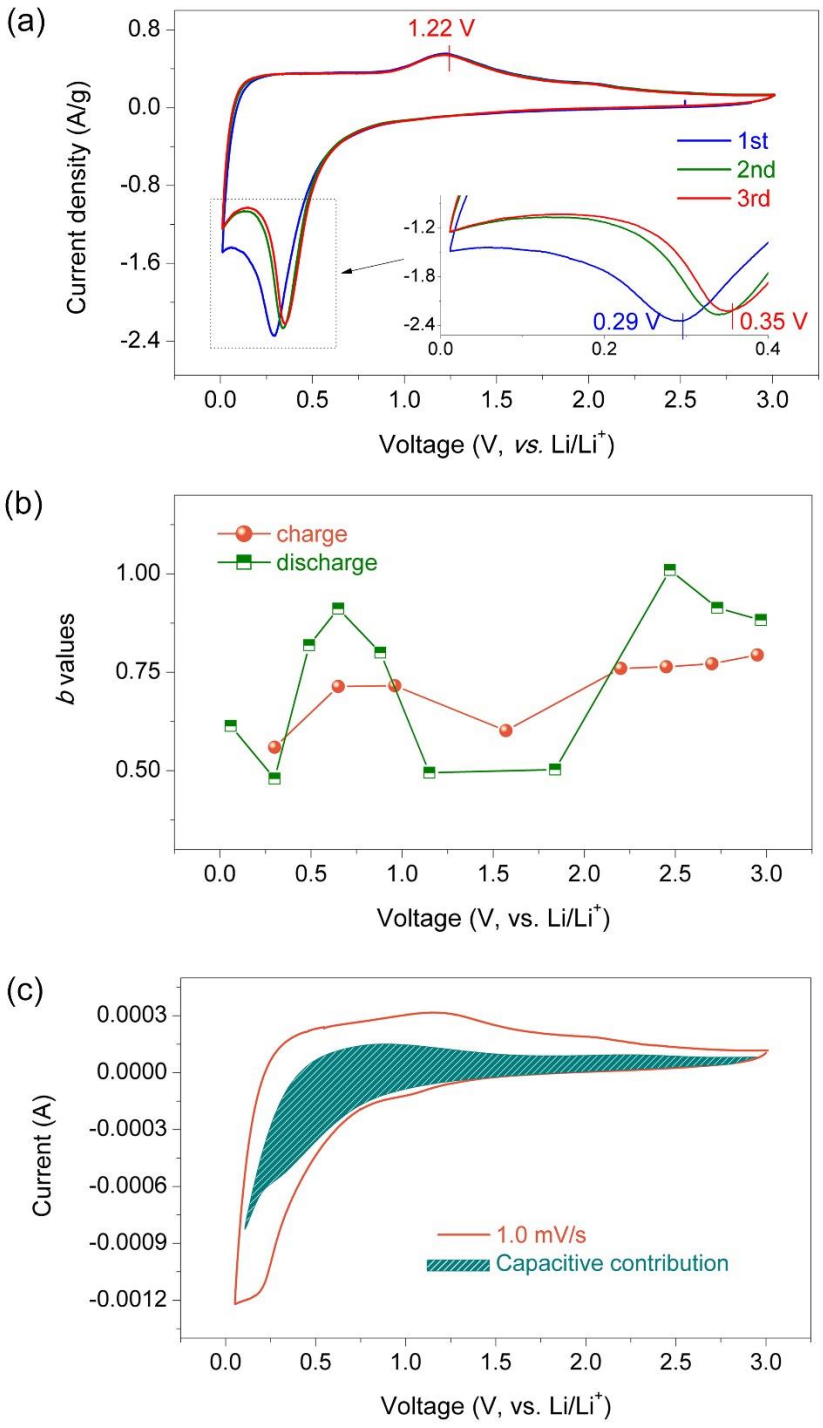

Figure 3. (a) Cyclic voltammogram curve of the MnO/C anode without the addition of conductive material in a Li-ion half cell where Li-ion metal was used as the counter electrode. The reducing peak around 0.35 V and the oxidizing peak at 1.22 V represent the conversion reaction of the MnO/C anode in the discharging and charging process, respectively. (b) *b*-values at various voltages. The data were calculated from CV curves at varying sweep rates and used to evaluate the diffusion or adsorption-controlled reaction process at different electrochemical stages. (c) The separated capacitive contribution (shaded area) of the total charge storage at a sweeping rate of 1 mV s^{-1}. The capacitive contribution is around 60 % of the total energy storage state.

In order to further understand the details of MnO/C anode kinetics, especially the ion diffusion and charge transfer in the charge/discharge process, EIS was adopted to record the change of impedance spectra at different electrochemical states in the 3rd cycle. The galvanostatic current density was set at 20 mA g^{-1} to ensure the reactions achieve equilibrium. The cell was allowed to rest for 20 min before collecting the EIS spectra at a voltage amplitude of 5 mV. Figure 4a shows the EIS spectra during the discharging process. Initially, the spectrum at 2.4 V consists of a semicircle at high frequency and a subsequent straight line at lower frequency. Before the voltage decreases below 1.2 V, all spectra are similar in shape, though the slope of the straight line is slightly different. However, there are two semicircles present when the voltage was lower than 1.0 V. The diameters of the semicircles gradually decrease when the voltage goes down. At 0.2 V, the spectrum displays the smallest two semicircles with a straight line. During the charging process, the spectra evolve from two semicircles with a linear tail to one semicircle and a linear tail (Figure S7a). The charging spectra at fixed voltages exhibit similar shapes and sizes as the results in discharging spectra, demonstrating good reversibility of the electrochemical reactions in the MnO/C electrode. In general, the EIS spectrum can be fit with an equivalent circuit that includes the resistance of the electrolyte (R_s), the resistance of the SEI film (R_f), charge transfer resistance (R_{ct}), constant phase element (CPE), and the Warburg resistance (Z_W). Li-ion diffusion coefficients of electrodes can be calculated from the low-frequency plots of EIS spectra based on the following equations [39]

$$Z' = R_s + R_f + R_{ct} + \sigma_w \omega^{-0.5} \quad (8)$$

$$D_{Li^+} = R^2T^2/2A^2n^4F^4C^2\sigma_w^2 \quad (9)$$

where ω, A, n, F, C, R, and T stands for the angular frequency, electrode area (0.50 cm^2), reactive electron number per chemical formula (2), Faraday's constant (96, 500 C mol^{-1}), the molar concentration of Li ions (1.0×10^{-3} mol cm^{-3}), gas constant (8.314 J $mol^{-1} \cdot K^{-1}$), and the

testing temperature (298 K), respectively. It is noting that Li-ion concentration was assumed as the same of electrolyte and stayed constantly owing to Li metal anode provided sufficient Li ions for the electrochemical reaction. The Warburg coefficient (σ_w) was obtained from the slopes of $Z'-\omega^{-1/2}$ curves as shown in Figure S7b-c. The ion diffusion coefficients are shown in Figure 4b. At different stages of charge/discharge, the MnO/C electrode has different ion diffusion coefficients. The fully charged state at 3.0 V has the lowest coefficient of ~10^{-15} cm^2 s^{-1} and the fully discharged state at 0.01 V has the highest coefficient of ~10^{-11} cm^2 s^{-1}, which is higher than commercial and other nanostructured MnO at the same voltages because its smaller particle size (~6 nm) of MnO and higher electrical conductivity (106 S/m) of carbon coating in comparison with other nanostructured MnO composite, such as mesocrystal MnO that has a particle size around 10 nm and electrical conductivity of 2.97×10^{-3} S/cm.[39] Furthermore, the charged state at a fixed voltage displays a slightly higher coefficient than that of the discharged state. The possible reason for the large coefficient difference at fully charged and discharged states can be attributed to the phase compositions of the MnO/C electrode. In the fully charged state, the phase is cubic MnO, which has a strong ionic chemical bond (Mn-O, 402 kJ mol^{-1})[37] and a high atomic packing density (~68%) making it difficult for the Li-ion to diffuse through the crystal body. However, in the fully discharged state, there are metallic Mn and Li_2O. Aside from the relatively weak chemical bond of Li-O (341 kJ mol^{-1}),[37] the products in the fully discharged state are in the amorphous state or local short-range ordered arrangement,[52,31] meaning they are loosely packed. Thus, the working ions can easily migrate through the open spaces or channels. The EIS spectra at 0.2, 0.8 and 2.6 V in the charge/discharge states are plotted together to compare and analyze the effects of the phase compositions in the electrode (Figure 4c-d). A schematic of phase evolution and equivalent circuits are shown in Figure 4e-f. At the initial discharge process, the phase at 2.6 V is MnO and the semicircle in the EIS spectrum stems from the resistance (104 Ω) corresponding to the charge transfer in MnO, which agrees with the reported MnO anode at the charging state.[24, 52, 59] When voltage decreases to 0.8 V, two semicircles appear as per the literature.[60] The one at the higher frequency still relates to the charge transfer resistance (60 Ω) but the other semicircle of lower frequency correlates to the resistance from the SEI film (145 Ω). Based on the brick-layer model,[61] the capacitances of nanoparticles

(CPE1) is far smaller than the capacitances from the interfaces between the SEI and MnO particles (CPE_2) because the width of interface is smaller than particle size. The simulated results listed in Table 2 strongly support this argument. The increase of the resistance at 0.8 V can be attributed to the formation of a SEI accompanied with the decomposition of the electrolyte and the breakdown of MnO. Additionally, the disordered atoms scatter the charges leading to an increase in the resistance. At the discharge state of 0.2 V, both resistances became smaller. The possible reason for this is that the metallic Mn precipitated homogenously to form a conductive network in the electrode. Additionally, the composition of the SEI gradually changes, benefiting the formation of Li_2CO_3 by increasing the charge transfer and ion migration but mitigating the LiF formation owing to its insulating property.[62-64] In the reverse charging process, similar EIS spectra at 0.2 V with the comparable resistances at the discharge state of 0.2 V, indicating similar chemical surroundings in the electrode. When the voltage increases to 0.8 V, the R_{ct} and R_f are larger than those of the same discharge state. The possible reason is that the partial decomposition of the SEI and Li_2O leads to the disappearance of electronic and ionic components, resulting in the increased resistances. LiF, an electronic insulator, needs a high decomposition voltage of 6.1 V to break its strong ionic bond if the system cannot provide enough driving force.[65] When charged to 2.6 V, the R_{ct} is around 126 Ω, which is higher than that of 104 Ω at the same discharge voltage, suggesting a slightly high-resistance component remains in the system or a slight change on the particle surface that is not fully recovered. The similar EIS spectra under the same charge and discharge voltage and the change of the number of semicircles under different voltage suggest a nearly reversible SEI owing to the capacitances from SEI occur and then disappear in the discharge and charge process. The reason is that the compositions of SEI and electrode materials have different dielectric constants that lead to a big difference in capacitances as shown in Table 2. In the charge process, the second semicircle at middle frequencies disappear, meaning one interface disappears. In fact, the solid electrode material which cannot disappear, probably corresponds to the SEI layer. This reversible SEI play a role in ion and electron storage reservoir that allows for the high specific capacity and ensures a stable cycling performance. The gradually increased ion diffusion coefficient during the discharge process accelerates the electrode reactions and enhances the rate capability. It

is worth noting that the nanostructured MnO/C anode still favors high ion migration, but the reaction is controlled by diffusion at low voltages, such as at 0.3 V.

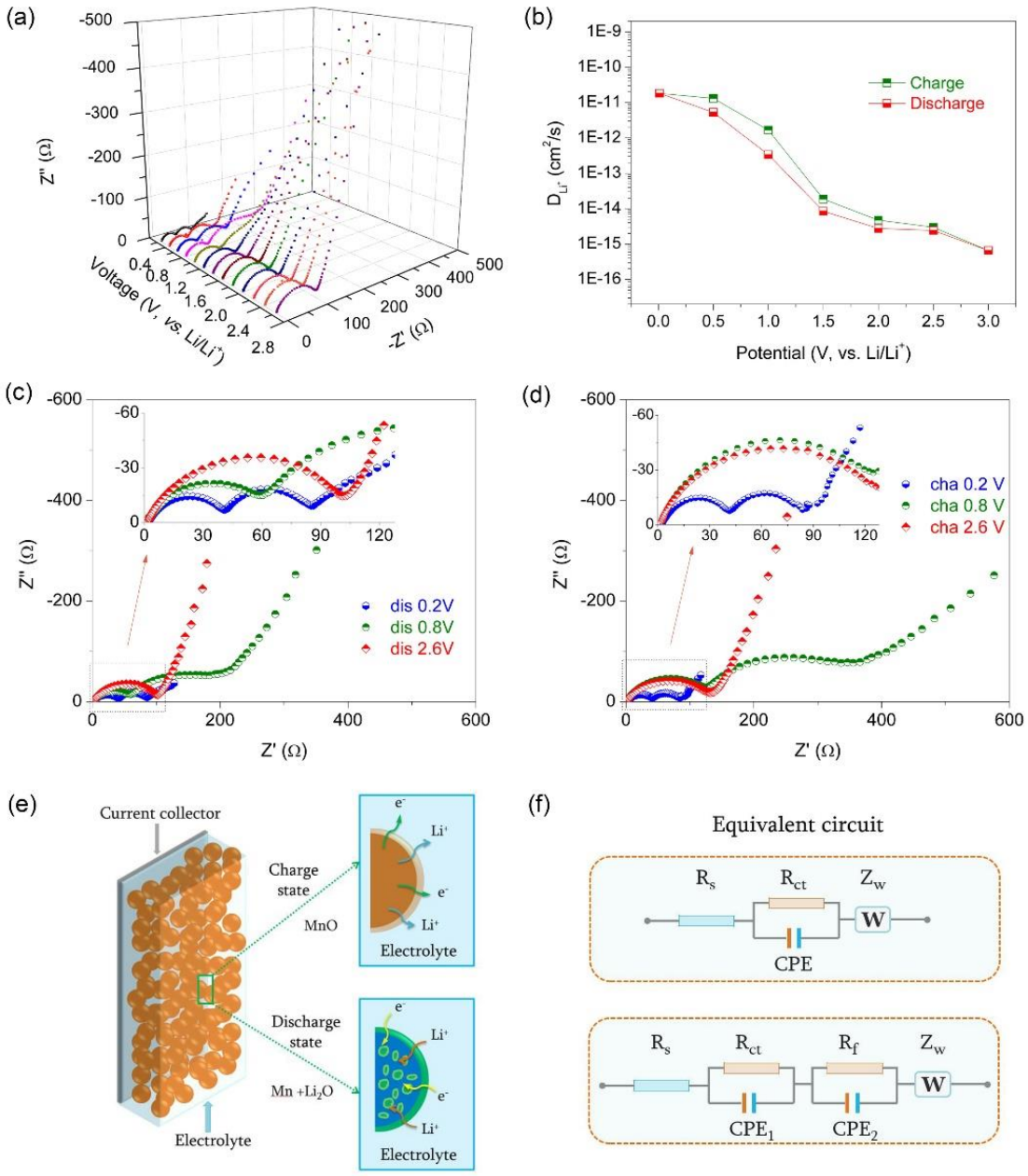

Figure 4. (a) Electrochemical impedance spectra at different discharge stages. The semicircle changes from one to two when the potential decreases from a fully charged state (3.0 V) to a fully discharged state (0.01 V). (b) The Li-ion diffusion coefficients of the MnO/C anode under different electrochemical potentials. The difference between the coefficient of the fully charged and discharged states stems from the varying phase compositions. (c) A comparison of the EIS spectra from different discharge potentials versus Li/Li+. The resistances from the semicircles present a remarkable variation, especially when the formation of solid electrolyte interphase starts around 0.8 V owing to the decomposition of the electrolyte. (d) EIS spectra at various charging stages. The resistances at 0.8 V increase more than that collected at a discharging state, implying a reaction hysteresis between the charging and discharging states at the same electrochemical potential. (e) Schematic of the phase transition and composition of the charging and discharging

states. The formation of a SEI and the precipitation of metallic Mn change the chemical compositions and states of the whole electrode. (f) The equivalent circuit for EIS spectra at different states. An additional circle in the EIS suggests a parallel resistance (R) and constant phase element (CPE) in the equivalent circuit and a new interphase is formed in the electrode.

Table 2. The Resistances (R_s, R_{ct}, and R_f) and Capacitances ($CPE1$, $CPE2$)

States	Voltage (V)	R_s (Ω)	R_{ct} (Ω)	R_f (Ω)	$CPE1$ (F)	$CPE2$ (F)
Discharge	2.6	2.5	104	-	2.13×10^{-5}	-
	0.8	2.6	66	173	3.01×10^{-5}	1.68×10^{-3}
	0.2	2.5	42	53	3.12×10^{-5}	1.57×10^{-3}
Charge	0.2	2.3	44	53	4.70×10^{-5}	1.82×10^{-3}
	0.8	2.7	135	234	1.49×10^{-5}	9.35×10^{-4}
	2.6	2.5	142	-	5.00×10^{-5}	-

Performances in Li-ion Capacitor

The electrochemical potential and diffusivity of electrode materials have significant impacts on the performances of a device, especially the energy density and efficiency. Choosing a stable cathode with a slight or no voltage hysteresis can effectively reveal the true performance of MnO/C in a full cell. Activated carbon (AC) has excellent chemical stability and a high specific surface area so it is generally used in electrodes for supercapacitors.[66] A commercial AC derived from a coconut shell with a specific surface area around 1,800 $m^2 g^{-1}$ was adopted as a cathode to build a Li-ion capacitor with MnO/C as the anode (Figure 5a). A Celgard polymer film and packaged porous Li metal foil was used to separate the cathode and anode as well as to compensate for the Li consmption during the first lithiation of the MnO/C anode as well as to avoid the complex process for preparing a pre-lithiated anode and an assembly capacitor in two steps.[67] In the half cells, the AC cathode has a maximum voltage of 4.5 V and the MnO/C anode reaches a minimum voltage of 0.01 V *versus* Li/Li^+ (Figure 5b). Taking into consideration the discharge voltage plateau of the MnO/C anode around 0.5 V, the working window of the capacitor was set to 0.1-4.0 V. The capacitor ran over 20 cycles at a current density of 0.1 A g^{-1} to activate the anode (Figure 5c). The initial capacity was 405 mAh g^{-1} with a Coulombic efficiency of 75% meaning that lithiation of the anode consumed Li ions, forming an SEI. In the following cycles, the Coulombic efficiency stayed at 100% and the

specific capacity slightly increased. Even when the current density increased to 25.6 A g^{-1}, the capacitor still delivered a specific capacity of 57 mAh g^{-1} within 9 s, reaching a high-power density of 11,160 W kg^{-1}. When the current density returned to 0.1 A g^{-1}, the capacity was very similar to the initial capacity. The capacitor was cycled at 5 A g^{-1} for 1000 cycles and the specific capacity maintained at around 300 mAh g^{-1} and displayed an undetected degradation during the long-term cycling process (Figure 5d). This excellent cycling stability exhibits a huge competitive advantage in comparison to the reported Li-ion capacitors, such as the VN//AC,[68] MnO//CNS,[27] and TiC//AC [69] systems. The energy efficiency of Li-ion batteries is defined as the ratio between the discharge and charge energy densities.[70] The energy efficiency of the MnO/C//AC capacitor reaches 90% at a current density of 0.1 A g^{-1}, which is slightly lower than the value of 95% for the $Li_3V_2(PO_4)_3$//$Li_4Ti_5O_{12}$ battery.[70] The reason for the lower energy efficiency stems from the voltage polarization of the anode, because the discharge energy density of the capacitor is the area encompassed by the charge voltage curve of the anode and the discharge voltage curve of the cathode.[5] This work shows that discovering the reasons behind the voltage profiles is valuable for designing desirable electrode materials and fabricating high-efficiency energy storage devices.

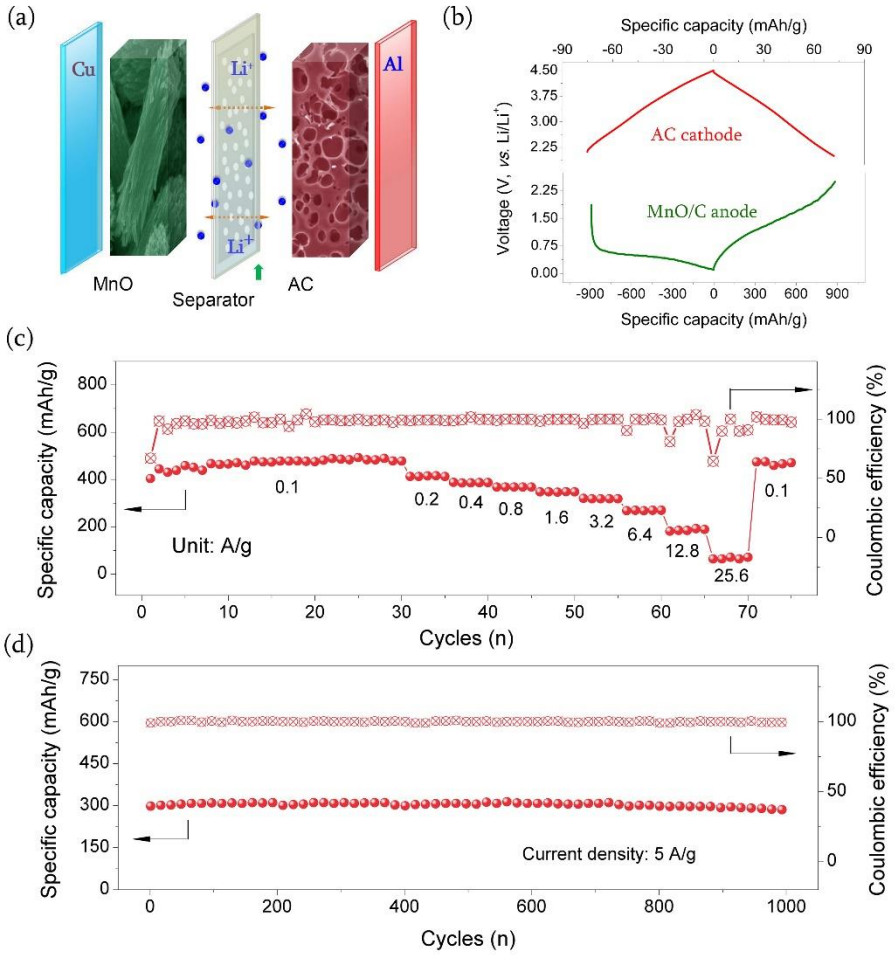

Figure 5. (a) Schematic configuration of the hybrid Li-ion battery. The MnO/C anode and activated carbon cathode is separated by a Celgard polymer separator and packaged porous Li metal for compensating the Li ion consumption of the anode during the first cycles. (b) The voltage profiles of both electrodes and their working windows. The voltage difference between the cathode and anode is the maximum voltage window of the full capacitor. (c) The rate capability of the MnO/C//AC hybrid capacitor within a working voltage window of 0.1-4.0 V. The capacitor at 25.6 A g^{-1} can deliver a power density of 11,160 W kg^{-1} within 9 s. (d) The cycling stability of the hybrid capacitor at a current density of 5 A g^{-1} shows no degradation over 1000 cycles.

Conclusions

The thermodynamics calculation and crystal field analysis revealed that the bond dissociation energy correlates with the discharge potential of MnO. The different electron ordering of split 3*d* orbitals determines the potential profiles and the energy difference from the t_{2g} and e_g orbitals leads to the potential hysteresis in the charge/discharge process. For the MnO/C anode, the diffusion and surface reaction contribution were found to vary significantly at the different charge/discharge states; Li ion diffusion

coefficient changed from ~10^{-15} cm^2 s^{-1} at the fully charged state to ~10^{-11} cm^2 s^{-1} at the fully discharged state. The continuous changing phase compositions, especially the precipitated Mn and partially amorphous oxide, are likely to reduce the charge transfer resistance and enhance the ion migration during the discharging process. The high specific surface area and smaller size of MnO/C nanostructures allowed us to achieve the high reversible capacity of 1018 mAh g^{-1} with the capacitance contribution of around 60%, and an energy storage efficiency of 90% was attained in a MnO/C//AC capacitor. These fundamentals on ionic diffusion and electrochemical potential and the practical example are helpful to understand a given material and help us design and/or tune a desired material for high efficient energy storage.

Conflicts of interest

There are no conflicts to declare.

Acknowledgements

This work was supported by the National Science Foundation (DMR No.1505902, No.1803256). Part of this work was conducted at the Molecular Analysis Facility, a National Nanotechnology Coordinated Infrastructure site at the Clean Energy Institute in University of Washington (Grant ECC1542101).

References

1 D. Larcher and J. M. Tarascon, *Nat. Chem.*, 2015, **7**, 19-29.
2 J. B. Goodenough, *Energy Storage Mater.*, 2015, **1**, 158-161.
3 H. D. Yoo, E. Markevich, G. Salitra, D. Sharon and D. Aurbach, *Mater. Today*, 2014, **17**, 110-121.
4 S. Goriparti, E. Miele, F. De Angelis, E. Di Fabrizio, R. Proietti Zaccaria and C. Capiglia, *J.Power Sources*, 2014, **257**, 421-443.
5 C. Liu and G. Cao, in *Nanomaterials for Energy Conversion and Storage*, eds. D. Wang and G. Cao, WORLD SCIENTIFIC (EUROPE), 2018, DOI: doi:10.1142/9781786343635_0010, pp. 397-451.
6 N. Nitta, F. Wu, J. T. Lee and G. Yushin, *Mater. Today*, 2015, **18**, 252–264.
7 R. C. Massé, C. Liu, Y. Li, L. Mai and G. Cao, *Nat. Sci. Rev.*, 2017, **4**, 26-53.
8 M. Ashuri, Q. R. He and L. L. Shaw, *Nanoscale*, 2016, **8**, 74-103.

9 S. Wu, C. Han, J. Iocozzia, M. Lu, R. Ge, R. Xu and Z. Lin, *Angew. Chem. Int. Edit*, 2016, **55**, 7898-7922.
10 N. Nitta and G. Yushin, *Part. Part. Syst. Char.*, 2014, **31**, 317-336.
11 M. N. Obrovac and V. L. Chevrier, *Chem. Rev.*, 2014, **114**, 11444-11502.
12 P. Poizot, S. Laruelle, S. Grugeon, L. Dupont and J. M. Tarascon, *Nature*, 2000, **407**, 496-499.
13 F. Wang, S.W. Kim, D.H. Seo, K. Kang, L. Wang, D. Su, J. J. Vajo, J. Wang and J. Graetz, *Nat. Commun.*, 2015, **6**, 6668.
14 J. Cabana, L. Monconduit, D. Larcher and M. R. Palacín, *Adv. Mater.*, 2010, **22**, E170-E192.
15 F. Wu and G. Yushin, *Energy Environ. Sci.*, 2017, **10**, 435-459.
16 M. V. Reddy, G. V. S. Rao and B. V. R. Chowdari, *Chem. Rev.*, 2013, **113**, 5364-5457.
17 Y. Xiao, S. H. Lee and Y.K. Sun, *Adv. Energy Mater.*, 2017, **7**, 1601329.
18 X. Wang, H.M. Kim, Y. Xiao and Y.K. Sun, *J. Mater. Chem.A*, 2016, **4**, 14915-14931.
19 T. Lu, S. M. Dong, C. J. Zhang, L. X. Zhang and G. L. Cui, *Coord. Chem. Rev.*, 2017, **332**, 75-99.
20 L. Liu, X. Yang, C. Lv, A. Zhu, X. Zhu, S. Guo, C. Chen and D. Yang, *ACS Appl. Mater. Interfaces*, 2016, **8**, 7047-7053.
21 K. Adpakpang, X. Jin, S. Lee, S. M. Oh, N.S. Lee and S.J. Hwang, *ACS Appl. Mater. Interfaces*, 2016, **8**, 13360-13372.
22 W. Eom, A. Kim, H. Park, H. Kim and T. H. Han, *Adv. Funct. Mater.*, 2016, **26**, 7605-7613.
23 Y. Sun, X. Hu, W. Luo, F. Xia and Y. Huang, *Adv. Funct. Mater.*, 2013, **23**, 2436-2444.
24 H. Jiang, Y. Hu, S. Guo, C. Yan, P. S. Lee and C. Li, *ACS Nano*, 2014, **8**, 6038-6046.
25 K. Su, C. Wang, H. G. Nie, Y. Guan, F. Liu and J. T. Chen, *J. Mater. Chem.A*, 2014, **2**, 10000-10006.
26 C. Liu, C. Zhang, H. Song, X. Nan, H. Fu and G. Cao, *J. Mater. Chem.A*, 2016, **4**, 3362-3370.
27 H. L. Wang, Z. W. Xu, Z. Li, K. Cui, J. Ding, A. Kohandehghan, X. H. Tan, B. Zahiri, B. C. Olsen, C. M. B. Holt and D. Mitlin, *Nano Lett.*, 2014, **14**, 1987-1994.
28 S.-H. Yu, X. Feng, N. Zhang, J. Seok and H. D. Abruña, *Accounts Chem. Res.*, 2018, **51**, 273-281.
29 W.M. Zhang, X.L. Wu, J.S. Hu, Y.G. Guo and L.J. Wan, *Adv. Funct. Mater.*, 2008, **18**, 3941-3946.
30 X. Jiang, W. Yu, H. Wang, H. Xu, X. Liu and Y. Ding, *J. Mater. Chem.A*, 2016, **4**, 920-925.
31 M. M. Butala, K. R. Danks, M. A. Lumley, S. Zhou, B. C. Melot and R. Seshadri, *ACS Appl. Mater. Interfaces*, 2016, **8**, 6496-6503.
32 K. Zhong, X. Xia, B. Zhang, H. Li, Z. Wang and L. Chen, *J.Power Sources*, 2010, **195**, 3300-3308.
33 G. Yoon, D. H. Kim, I. Park, D. Chang, B. Kim, B. Lee, K. Oh and K. Kang, *Adv. Funct. Mater.*, 2017, **27**, 1702887.
34 C. Liu, Z. G. Neale and G. Cao, *Mater. Today*, 2016, **19**, 109-123.
35 H. Li, P. Balaya and J. Maier, *J. Electrochem. Soc.*, 2004, **151**, A1878-A1885.
36 J. Gao, S.Q. Shi and H. Li, *Chinese Phys. B*, 2016, **25**, 018210.

37 J. G. Speight, *Lange's Handbook of Chemistry, 70th Anniversary Edition 16th Edition*, McGraw-Hill Professional, 2005.
38 G. Trimarchi, Z. Wang and A. Zunger, *Phys. Rev. B*, 2018, **97**, 035107.
39 C. Liu, C. Zhang, H. Song, C. Zhang, Y. Liu, X. Nan and G. Cao, *Nano Energy*, 2016, **22**, 290-300.
40 W. D. Callister, *Fundamentals of Materials Science and Engineering*, John Wiley & Sons, Inc., 2001.
41 C. Liu, C. Zhang, H. Fu, X. Nan and G. Cao, *Adv. Energy Mater.*, 2017, **7**, 1601127.
42 X. Nan, C. Liu, K. Wang, W. Ma, C. Zhang, H. Fu, Z. Li and G. Cao, *J. Materiomics*, 2016, **2**, 350-357.
43 Y. Zhou, S. L. Candelaria, Q. Liu, Y. Huang, E. Uchaker and G. Cao, *J. Mater. Chem.A*, 2014, **2**, 8472-8482.
44 T. Jawhari, A. Roid and J. Casado, *Carbon*, 1995, **33**, 1561-1565.
45 T. Brezesinski, J. Wang, J. Polleux, B. Dunn and S. H. Tolbert, *J. Am. Chem. Soc.*, 2009, **131**, 1802-1809.
46 Y. Zhu, L. Peng, D. Chen and G. Yu, *Nano Lett.*, 2016, **16**, 742-747.
47 S. Huang, L. Zhang, X. Lu, L. Liu, L. Liu, X. Sun, Y. Yin, S. Oswald, Z. Zou, F. Ding and O. G. Schmidt, *ACS Nano*, 2017, **11**, 821-830.
48 B. E. Conway, V. Birss and J. Wojtowicz, *J.Power Sources*, 1997, **66**, 1-14.
49 J. Wang, J. Polleux, J. Lim and B. Dunn, *J. Phys. Chem. C*, 2007, **111**, 14925-14931.
50 H. S. Kim, J. B. Cook, H. Lin, J. S. Ko, S. H. Tolbert, V. Ozolins and B. Dunn, *Nat. Mater.*, 2017, **16**, 454-460.
51 J. Mei, T. F. Yi, X. Y. Li, Y. R. Zhu, Y. Xie and C. F. Zhang, *ACS Appl. Mater. Interfaces*, 2017, **9**, 23662-23671.
52 Y. Xia, Z. Xiao, X. Dou, H. Huang, X. Lu, R. Yan, Y. Gan, W. Zhu, J. Tu, W. Zhang and X. Tao, *ACS Nano*, 2013, **7**, 7083-7092.
53 S. Laruelle, S. Grugeon, P. Poizot, M. Dollé, L. Dupont and J.-M. Tarascon, *J. Electrochem. Soc.*, 2002, **149**, A627-A634.
54 A. Ponrouch, P.-L. Taberna, P. Simon and M. R. Palacín, *Electrochim. Acta*, 2012, **61**, 13-18.
55 G. C. Chung, H. J. Kim, S. I. Yu, S. H. Jun, J. w. Choi and M. H. Kim, *J. Electrochem. Soc.*, 2000, **147**, 4391-4398.
56 S. J. An, J. Li, C. Daniel, D. Mohanty, S. Nagpure and D. L. Wood Iii, *Carbon*, 2016, **105**, 52-76.
57 Y. M. Zhao, Y. P. Cui, J. Shi, W. Liu, Z. C. Shi, S. G. Chen, X. Wang and H. L. Wang, *J. Mater. Chem.A*, 2017, **5**, 15243-15252.
58 X. Tang, G. Sui, Q. Cai, W. Zhong and X. Yang, *J. Mater. Chem.A*, 2016, **4**, 2082-2088
59 L. Sheng, S. Liang, T. Wei, J. Chang, Z. Jiang, L. Zhang, Q. Zhou, J. Zhou, L. Jiang and Z. Fan, *Energy Storage Mater.*, 2018, **12**, 94-102.
60 G. Carbonari, F. Maroni, M. Pasqualini, R. Tossici and F. Nobili, *Electrochim. Acta*, 2017, **247**, 392-399.
61 J. T. S. Irvine, D. C. Sinclair and A. R. West, *Adv. Mater.*, 1990, **2**, 132-138.
62 E. Peled and S. Menkin, *J. Electrochem. Soc.*, 2017, **164**, A1703-A1719.
63 S. Shi, Y. Qi, H. Li and L. G. Hector, *J. Phys. Chem. C*, 2013, **117**, 8579-8593.

64 J. Mizusaki, H. Tagawa, K. Saito, K. Uchida and M. Tezuka, *Solid State Ion.*, 1992, **53-56**, 791-797.
65 H. Li, G. Richter and J. Maier, *Adv. Mater.*, 2003, **15**, 736-739.
66 M. Sevilla and R. Mokaya, *Energy Environ. Sci.*, 2014, **7**, 1250-1280.
67 W. J. Cao and J. P. Zheng, *J.Power Sources*, 2012, **213**, 180-185.
68 R. Wang, J. Lang, P. Zhang, Z. Lin and X. Yan, *Adv. Funct. Mater.*, 2015, **25**, 2270-2278.
69 H. Wang, Y. Zhang, H. Ang, Y. Zhang, H. T. Tan, Y. Zhang, Y. Guo, J. B. Franklin, X. L. Wu, M. Srinivasan, H. J. Fan and Q. Yan, *Adv. Funct. Mater.*, 2016, **26**, 3082-3093.
70 C. Liu, S. Wang, C. Zhang, H. Fu, X. Nan, Y. Yang and G. Cao, *Energy Storage Mater.*, 2016, **5**, 93-102.